Compressive properties of pristine and SiC-Te-added MgB_2 powders, green compacts and spark-plasma-sintered bulks

[1,*]Petre Badica, [2]Dan Batalu, [1]Mihail Burdusel, [1,2]Mihai A. Grigoroscuta, [1]Gheorghe V. Aldica, [1]Monica Enculescu, [3]Raluca A. Gabor, [4]Zhiyong Wang, [4]Ruoxuan Huang, [4,5]Peifeng Li

[1] National Institute of Materials Physics, street Atomistilor 405 A, 077125 Magurele, Romania
[2]Faculty of Materials Science and Engineering, University Politehnica of Bucharest, Splaiul Independentei 313, 060042 Bucharest, Romania
[3] National Institute for Research in Chemistry, Splaiul Independentei 202, 060021, Bucharest, Romania
[4] School of Mechanical and Aerospace Engineering, Nanyang Technological University, Singapore
[5] School of Engineering, University of Glasgow, Glasgow G12 8QQ, U.K.

*contact address:
Petre Badica
National Institute of Materials Physics, street Atomistilor 405 A, 077125 Magurele, Romania
Fax: +40-21-3690177
Ph: +40-21-3690185
badica2003@yahoo.com

Submitted to Ceramics International, Elsevier

Compressive properties of pristine and SiC-Te-added MgB_2 powders, green compacts and spark-plasma-sintered bulks

[1,*]Petre Badica, [2]Dan Batalu, [1]Mihail Burdusel, [1,2]Mihai A. Grigoroscuta, [1]Gheorghe V. Aldica, [1]Monica Enculescu, [3]Raluca A. Gabor, [4]Zhiyong Wang, [4]Ruoxuan Huang, [4,5]Peifeng Li

[1] National Institute of Materials Physics, street Atomistilor 405 A, 077125 Magurele, Romania

[2]Faculty of Materials Science and Engineering, University Politehnica of Bucharest, Splaiul Independentei 313, 060042 Bucharest, Romania

[3] National Institute for Research in Chemistry, Splaiul Independentei 202, 060021, Bucharest, Romania

[4] School of Mechanical and Aerospace Engineering, Nanyang Technological University, Singapore

[5] School of Engineering, University of Glasgow, Glasgow G12 8QQ, U.K.

Abstract

Pristine and (SiC+Te)-added MgB_2 powders, green and spark plasma sintered (SPS) compacts were investigated from the viewpoint of quasi-static and dynamic (Split-Hopkinson Pressure Bar, SHPB) compressive mechanical properties The amount of the additive (SiC+Te) was selected to be the optimum one for maximization of the superconducting functional parameters. Pristine and added MgB_2 show very similar compressive parameters (tan δ, fracture strength, Vickers hardness, others) and fragment size in the SHPB test. However, for the bulk SPSed samples the ratio of intergranular to transgranular fracturing ratio changes, the first one being stronger in the added sample. This is reflected in the quasi-static K_{IC} that is higher for the added sample. Despite this result, sintered samples are brittle and have roughly similar fragmentation behavior as for brittle engineering ceramics. In the fragmentation process, the composite

nature of our samples should be considered with a special focus on MgB_2 blocks (colonies) that show the major contribution to fracturing. The Glenn-Chudnovsky model of fracturing under dynamic load provides the closest values to our experimental fragment size data.

Key words: MgB_2; compressive properties; Split-Hopkinson pressure bar; fractography; fragmentation.

1. Introduction

MgB_2 is prized as a practical light-weight (relative density of 2.63 g/cm^3) superconductor [1] with a high potential of use in portable applications. MgB_2 was also proposed as a biomaterial [2] for fabrication of biodegradable devices and for other biomedical applications. As a superconductor or as a biomedical material, mechanical properties are important.

In general, mechanical properties of bulk MgB_2 are determined under static loads. They are shown to depend on the processing technology, additives and the quality of the sample. Namely, one has to consider the density, microstructure, phase composition, and the chemical composition of MgB_2 including substitutions, e.g. substitution of B by C. Indentation tests (Vickers hardness and fracture toughness), and room temperature bending strength tests are reported in refs. [3-10] and [11-14], respectively. Elastic constants of MgB_2 were calculated [15-17] or determined experimentally [18-20], and they are consistent with each other. The maximum measured values of Young modulus E, fracture toughness K_{IC}, Vickers hardness $HV_{>9.8N}$ and four-point bending strength $\sigma_{4\text{-point bending}}$ are 313 ± 9 GPa for pristine MgB_2 [10] (273 GPa from resonant ultrasound spectroscopy [18]) and ~240 GPa for C-substituted MgB_2 ($MgB_{2-x}C_x$, x=0.1-0.3) [10], 4.4 ± 0.04 MPa·m$^{0.5}$ for pristine and 7.6 ± 2 MPa·m$^{0.5}$ for Ta-added MgB_2 [3], 14.94±0.52 GPa [10], and 278 ± 43 MPa [12], respectively. The last two indicated values are for pristine MgB_2. It is worthy to note that even pristine MgB_2 bulk samples are usually composites containing secondary phases such as higher Mg-borides, Mg- and B- oxides.

MgB_2 is recognized as a material with a brittle behavior [10]. Previous paragraph indicates that quasi-static mechanical parameters, although inferior to typical light-weight and brittle engineering materials (such as e.g. Al_2O_3 with relative density of 3.95 g/cm^3), are still competitive and recommend MgB_2 as a potentially useful light-weight structural material. To target the already addressed applications or new ones, further exploration of the mechanical properties of MgB_2 is of high interest.

In this work we report compressive mechanical properties measured on pristine and SiC+Te co-added MgB_2 powders, green compacts and high density bulk samples prepared by spark plasma sintering (SPS). The added composition was selected considering our previous results and that critical current density is significantly higher than for the pristine sample [21]. SiC is a popular additive to MgB_2 [22] enhancing pinning. Addition of Te is also effectively providing pinning centers [23]. It also improves sintering processes towards a higher and more uniform density of the MgB_2 core from the powder-in-tube tapes [24]. Samples in powder form were subject to dynamic mechanical analysis (DMA). Quasi-static compressive tests were applied to green compacts. The two experiments are useful starting points in processing of sintered bulks and powder-in-tube tapes. We also present our results of quasi-static and dynamic (Split Hopkinson Pressure Bar, SHPB) tests on spark plasma sintered samples. Fractography and fragmentation details are discussed. It is worthy to note that for some superconducting applications, improvement of mechanical properties of MgB_2 tapes/wires and bulks is equally important to enhancement of superconducting functional parameters, but to the best of authors' knowledge, DMA on MgB_2 powders, quasi-static tests on green bodies and SHPB experiments on monolithic MgB_2 were not approached in literature.

2. Material and Methods

Commercial powders (Alfa Aesar) were used: MgB_2 (99.5 %, 1-2 μm), SiC nano-powder (Merck, 99% purity, 45 nm) and Te (C595090, Pierce Eurochemie B.V., 99.9999% purity, powder ground from a metal ingot). The MgB_2 powder contains, according to scanning electron microscopy (SEM), particles < 300 nm, agglomerated into larger aggregates up to 2-5 μm. The Te powder was composed of ~400 nm particles and large 2–10 μm blocks, as observed by SEM. The powders were mixed to obtain the composition $MgB_2(SiC)_{0.025}Te_{0.01}$. This composition was found to be the optimum one for maximization of the superconducting critical current density [21].

The pristine powder or the mixture with the indicated composition were loaded into a graphite die of ~2 cm inner diameter and sintered by SPS (FCT Systeme GmbH – HP D 5, Germany) for 3 minutes at 1150 °C. Vacuum in the SPS chamber was of 35 Pa. A uniaxial pressure of 95 MPa was applied on sample [7]. Our samples are denoted as follows: "MgB_2-pwd" for pristine MgB_2 powder, "MgB_2+SiC+Te-pwd" for MgB_2 powder mixed with SiC and Te additions, "MgB_2-green" for pressed pristine powder, "MgB_2+SiC+Te-green" for pressed MgB_2+SiC+Te powder, "MgB_2-SPS" for pristine sintered bulk, and "MgB_2+SiC+Te-SPS" for sintered MgB_2 with SiC and Te additions.

The apparent density (Table 1) of the sintered samples was measured by the Archimedes method. Relative densities were calculated as the ratio between the apparent and theoretical density [25], considering that samples contain MgB_2 (2.63 g/cm^3), MgB_4 (2.49 g/cm^3), MgO (3.58 g/cm^3), MgTe (3.86 g/cm^3), and Mg_2Si (1.988 g/cm^3).

The X-ray diffraction (XRD) spectra were taken with a Bruker-AXS D8 ADVANCE ($Cu_{K_{\alpha 1}}$-radiation, λ = 1.5406 Å) diffractometer. Rietveld refinement was performed and the weight fraction of each phase was determined with MAUD v.2.31 software [26]. The residual strain and the crystallite size (Table 1) by using the Williamson-Hall procedure [27] were calculated based on XRD data.

SEM images and energy dispersive X-ray spectroscopy (SEM-EDS) were observed with a Zeiss EVO50 microscope on surfaces of fractured samples.

A Quantum Design MPMS-7T was used to measure curves of magnetic moment versus temperature, $m(T)$, in zero field-cooling (ZFC) conditions. Pieces cut from the SPSed samples and fragments resulting after the SHPB dynamic impact test were investigated.

Dynamic mechanical analyses (DMA) of MgB_2 and MgB_2+SiC+Te powders were performed on DMA Q800, TA Instruments, at room temperature (RT) with a force rate of 0.05 N/min, from 0 to 9 N, and from RT to 300 ºC with a heating rate of 3 °C/min. Curves of strain and stiffness with time and temperature are presented in Fig. 1. Values of the compressive loss modulus E″ (viscous component) and

storage modulus E′ (elastic component) were obtained and their ratio E″/E′ defines the loss tangent tan(δ) (where δ = phase lag between stress and strain).

Compression quasi-static experiments on green bodies (diameter=10 mm, height=10 mm) were performed on Instron 3382, with a compression rate of 0.5 mm/min. Green bulks were obtained for a load of 50 kN (637 MPa).

Bulk SPSed samples were cut into cylinders (diameter = 4.0 mm, height = 4.0 mm) by wire electrical discharge machining. Samples were subject to uniaxial compression (Instron 5569) with a rate of 0.24 mm/min. The compression process of the samples was captured by a JAI (JAI Ltd., Japan) BM-500 GE high resolution camera to accurately track and measure the strain history.

Vickers hardness (*HV*) was measured on a polished surface of the SPSed sample for a load of 2 kgf (19.6 N) using a CV-400DTS Micro Hardness Tester. We applied the standard procedure according to ASTM C 1327-03. Ten measurements were performed with a dwell time of 10 s each. The average hardness and values of the standard deviation were determined (Table 1). Based on Vickers hardness and the induced cracks, we calculated the static fracture toughness K_{IC} (Table 1) according to ref. [28]:

$$K_{Ic} = 0.048 \cdot \left(\frac{\ell}{a}\right)^{-\frac{1}{2}} \cdot \left(\frac{HV}{E \cdot \Phi}\right)^{-\frac{2}{5}} \cdot \left(\frac{HV \cdot a^{\frac{1}{2}}}{\Phi}\right) \quad (1)$$

where: K_{Ic} = fracture toughness (MPa·m$^{1/2}$), ℓ = crack length (μm), a = indent half-diagonal (μm), HV = Vickers hardness (GPa), E = Young's modulus (GPa), Φ = constraint factor (≈ 3) [29]. Berkovich hardness was measured with an Agilent G200 nano indenter (Table 1).

Uniaxial dynamic compression test on SPSed samples (diameter = 4.0 mm, height = 4.0 mm) was conducted using a Split-Hopkinson Pressure Bar (SHPB), designed at NTU, Singapore. The apparatus consists of 20 mm diameter YAG300 maraging steel striker (length 400 mm), incident and transmitted (both 1200 mm long) bars. The incident and transmitted bars were instrumented with TML strain gauges (Tokyo Sokki Kenkyujo Co. Ltd., Japan, gauge factor of 2.11). Signals from strain gauges were used to calculate the stress and strain history based on the one-dimensional elastic bar wave theory for a pulse propagating in a uniform bar (SHPB theory) as described in ref. [30]. Hardened high strength steel plates

with impedance matching that of the bars were sandwiched between the bars and specimens to avoid the indentation of the bars [31]. In the analysis of the SHPB test, the longitudinal wave velocity of the maraging steel bars is $c_0 = \sqrt{E_0/\rho_0} = 4786$ m·s^{-1}, where Young's modulus $E_0 = 184$ GPa and density $\rho_0 = 8030$ kg·m^{-3}.

The dimensions of resulted fragments in the SHPB test were measured (width and length) using Gimp 2.8 and ImageJ 1.6 on SEM images. Statistical analysis was applied on 926 and 815 fragments that resulted from the SHPB impact test of the samples MgB_2-SPS, and MgB_2+SiC+Te-SPS, respectively. Statistical toolbox of MATLAB was used to calculate the lognormal distribution of the fragment sizes resulting after SHPB based on eq. 2.

$$y = \frac{1}{\sigma \cdot x \cdot \sqrt{2 \cdot \pi}} e^{\frac{-(\ln x - \mu)^2}{2 \cdot \sigma^2}} \quad (2)$$

where y is the *probability density function* (PDF), x is the random variable (here width/length), σ and μ are the standard variation and the mean value of ln x.

Table 1. Measured and calculated physical and mechanical properties of MgB_2 and $MgB_2(SiC)_{0.025}Te_{0.01}$ samples in the powder, green and SPSed states.

Test	**Property**	**"MgB_2-pwd"**	**"MgB_2+SiC+Te-pwd"**
XRD	*a* lattice parameter of MgB_2 [Å]	3.080(7)	3.080(7)
	c lattice parameter in MgB_2 [Å]	3.515(0)	3.515(0)
	q_{Carbon} in $Mg(B_{1-q}C_q)_2$	0.02	0.02
	Crystallite size of MgB_2 [nm]	78 ± 18	78 ± 18
DMA	tan(δ)	~0.05	~0.05
Test	**Property**	**"MgB_2-green"**	**"MgB_2+SiC+Te-green"**
Compression (static)	Average Young's modulus (up to (1)*) [GPa]	1.65	2.05
	Average toughness (integral energy) up to first crack (MPa)	19.45	12.3
	Average fracture strength (max. stress) (MPa)	28.15	32.75
	Average strain at maximum stress (%)	3.05	2.85

Test	**Property**	**"MgB_2-SPS"**	**"MgB_2+SiC+Te-SPS"**
Archimedes bulk density	Apparent density, ρ [kg/m^3]	2520	2620
	Relative density, [%]	95.7	98.5
Magnetization measurement	Midpoint critical temperature, $T_{c,midpoint}$ [K] after quasi-static compressive test / SHPB	37.8 / 37.4	35.4 / 35.1
XRD	*a* lattice parameter of MgB_2	3.082(4)	3.076(8)
	c lattice parameter in MgB_2	3.526(0)	3.525(8)
	q_{Carbon} in $Mg(B_{1-q}C_q)_2$	0.011	0.024
	Crystallite size of MgB_2 [nm]	125 ± 30	100 ± 25
	Residual strain of MgB_2 [%]	0.37	0.48
	Amount of MgB_2 [wt.%]	82.8	68.1
Indentation:Vickers, Load 19.61 N	Vickers Hardness, $HV_{19.61}$ [GPa]	10.7	11
	Fracture toughness, K_{Ic} [MPa·m$^{1/2}$] (eq. 1)	3.6	5.2
Indentation: Berkovich	Berkovich Hardness [GPa] of MgB_2 (colonies)	4.5±1.5	8.5±1.6
Compression (static)	Average Young's modulus, E [GPa] from compression/ nanoindentation measurement	122/ 138	147/ 161
	Average failure strength, σ_{max} [MPa]	732	740
Dynamic impact test (SHPB)	The arithmetic mean experimental fragment size after SHPB test: length (*L*)/ width (*W*), [μm]	80/ 61	83/ 55
	Fracture strength at (1)*, [MPa]	1210	1217
	Strain at (1)	0.03	0.03
	Fracture strength (max), σ_p [MPa]	1803	1830
	Strain at (max.) fracture strength, ε_p	0.15	0.17
	Longitudinal wave velocity, *c* [m/s] (eq. 4)	6958	7490
	Strain rate $\dot{\varepsilon}_0$ [s^{-1}]	2500	2800

(1)* denotes the occurrence of the first crack.

3. Results and Discussion

3.1 DMA on powders

Curves of DMA for samples MgB_2-pwd and MgB_2+SiC+Te-pwd are presented in Fig. 1. Strain and stiffness curves vs. time and temperature show some differences between pristine and added sample.

At short times (< 10-20 min) from the application of the compressive load (Fig. 1a), the MgB_2 in the pristine sample shows a slow decrease (plateau) of strain, while stiffness shows a maximum. For the added sample there is a steep decrease of the strain and a continuous increase of the stiffness. This result suggests that the additive promotes easy and gradual load-accommodation so that an initial stronger resistance to the movement of the piston as observed for the pristine sample does not occur. At longer times (20 -180 min) pristine and added powders show a similar behavior (curves are almost parallel) and the general trend is that the strain decreases with the tendency to saturate, while stiffness increases almost in a linear manner. We shall also note that jumps in the strain and stiffness curves are fewer for the added sample, and this observation supports the idea that the additive has a positive effect on powder compaction. Other additives such as cubic BN, and $Ge_2C_6H_{10}O_7$ were also found to help dynamic compaction of the MgB_2 powder. Results will be presented elsewhere.

Curves of strain and stiffness vs. temperature for pristine and added MgB_2 samples are similar (Fig. 1b). The encountered differences are:

(i) strain is slightly higher for the added sample,

(ii) stiffness for the added sample takes lower values in the entire studied temperature range (20 - 300 °C), and

(iii) the slope of the stiffness increase with temperature for the added sample is slightly lower than for the pristine MgB_2 powder.

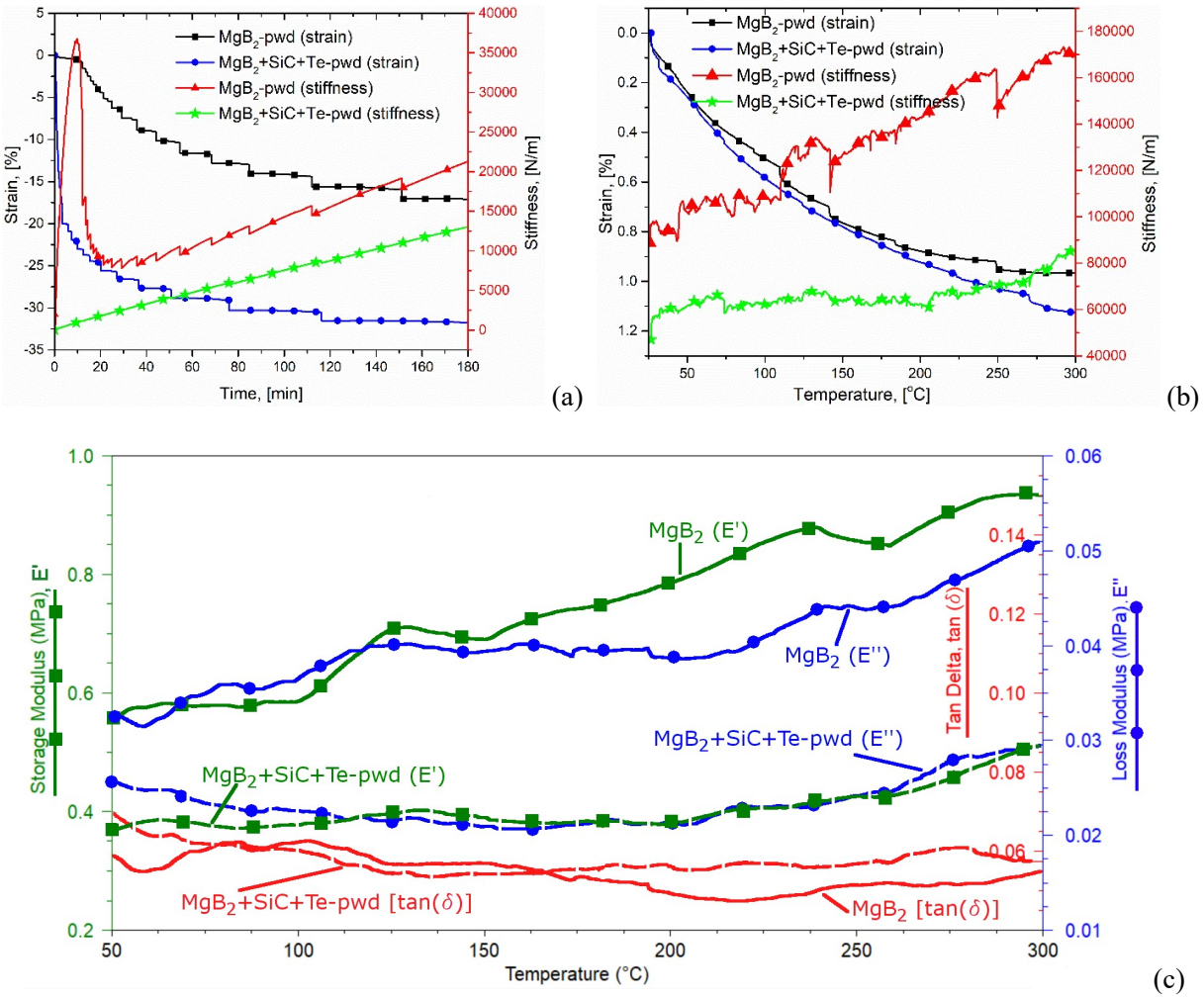

Fig. 1. Dynamically compressed powders of pristine and added MgB_2: (a) strain/stiffness vs. time at room temperature, (b) strain/stiffness vs. temperature, and (c) storage modulus E′, loss modulus E″, and tan(δ)=E″/E′ vs. temperature.

The differences (i) – (iii) are in good agreement with the idea that the additive aids MgB_2 powder compaction. Above ~170 °C, for the pristine sample (MgB2-pwd), the difference between the elastic component E′ and the viscous one E″ increases significantly, which is not the case for the added sample (MgB_2+SiC+Te-pwd). This is reflected in the somehow lower value of tan(δ) for the MgB_2-pwd than for MgB_2+SiC+Te-pwd, above ~170 °C, meaning that added sample has a stronger viscous behavior. Nevertheless, both powders show mainly an elastic behavior (E′ is large when compared with E″) leading

to small (around 0.05) and comparable values of tan(δ). The values of tan(δ) for each sample are weakly depending with temperature (50-300 °C).

Our results are thought to be useful for the MgB_2 powder-in-tube processing by mechanical deformation for fabrication of superconducting wires and tapes.

3.2 Quasi-static compression tests of green and Spark Plasma Sintered bulks

Green and SPSed bulks were tested by the quasi-static compression test. Stress-strain curves are presented in Fig. 2 and Table 1.

We observed in our previous work [7] that the green density of the MgB_2 compact influences evolution of the density during SPS and its final value when using fixed SPS processing conditions. Additives (type, amount, and morpho-structural specific features) also play an important role [32]. In the presence of additives, the dependence between green density and the final density of the sample after SPS requires a careful analysis. In the particular case of SiC and Te addition, bulks [21] (Table 1) and tapes processed by SPS [24] show an increased density when compared to pristine MgB_2 samples. Considering also results from Section 3.1 it is apparent that the additive (SiC+Te) has a favorable action on rheological properties of MgB_2 powder. However, in the case of SPS processing, the powder flow can be influenced by other processes such as pre-sintering and reactions occurring at high temperatures and the relationship between the densities of the green and sintered body is not a direct one. At temperatures of 900-1000 °C under hot isotropic pressing (HIP), DeFouw and Dunand [33] reported a superplastic compressive flow. A second aspect is that in the SPS processing an initial pressure has to be applied on the powder to ensure a good electrical contact between the sample and the mold system. Design of the pressure regime has to consider this aspect as well as the compression properties of the green body. Compression test of the green body performed in this work provides a reference point and can be used also for other pressure-assisted technologies.

Results of the quasi-static compression of the green bodies are presented in Table 1. For the "MgB_2-green" sample the average toughness up to the 1st crack and the strain at maximum stress are larger, Young's modulus and the maximum average compression strength (stress) are smaller than those for the "MgB_2+SiC+Te-green" sample. This result may indicate that the additive promotes a stronger resistance of the green sample to compression loading. This result can be understood through a better compaction (into a green body) of the added powder as noted in *Section 3.1*.

The average compressive failure strength and Young's modulus of the sintered bulks are slightly higher for the added samples. It suggests that pristine MgB_2 samples have a slightly higher ductility than the added samples. Nevertheless, stress-strain curves are typical for brittle fracturing, i.e. they are initially linear and end with a sudden drop of the stress at the break point. Brittle fracture can be also observed from Fig. 3.

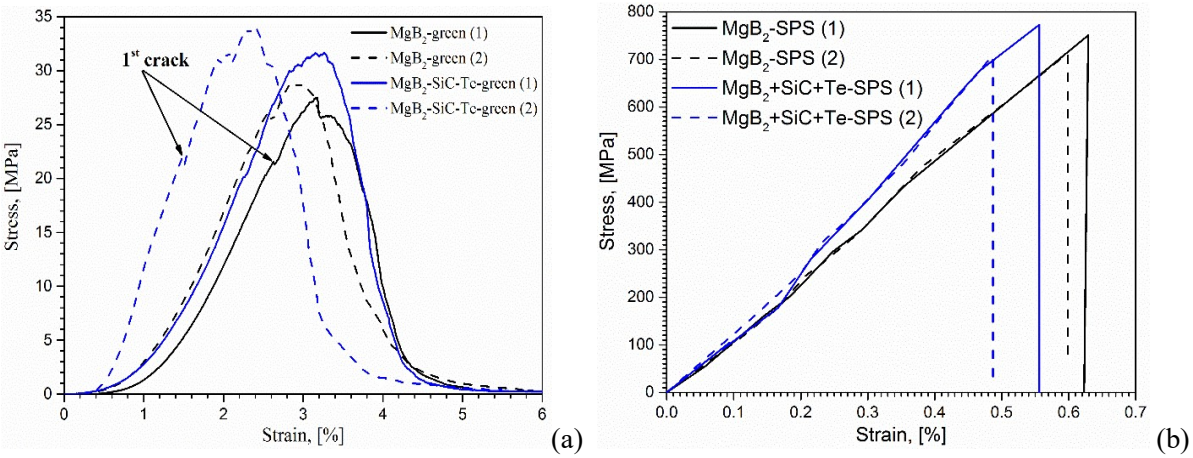

Fig. 2. Compression characteristic curves of pristine and added MgB_2 samples: (a) green samples, (b) sintered bulks.

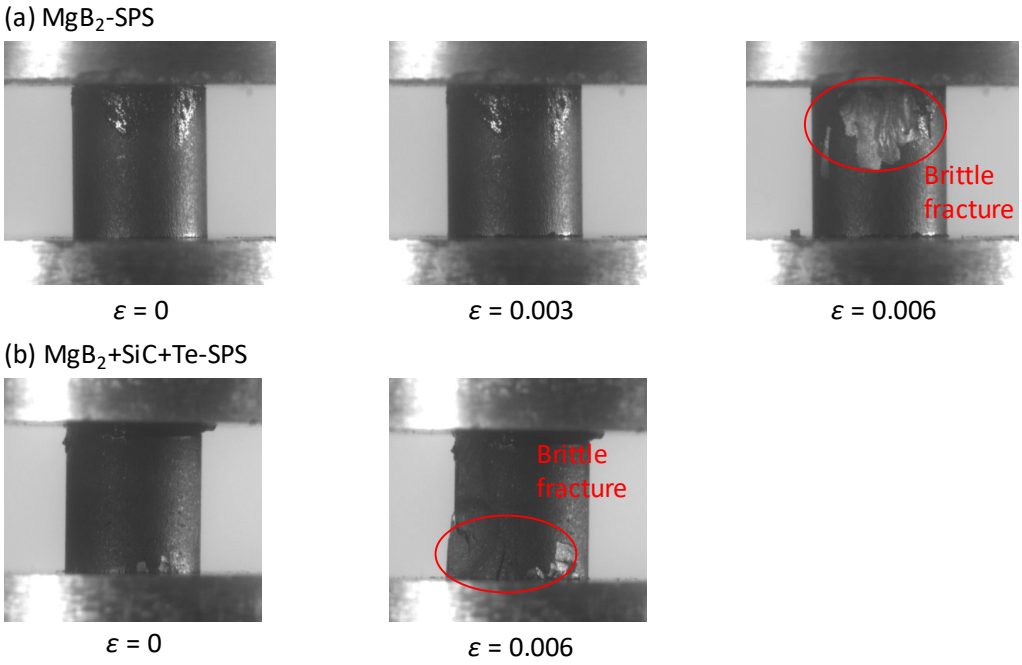

Fig. 3 Images taken at different measured strains during compressive test of the SPSed samples (a) pristine and (b) added MgB_2.

The high-resolution images taken during the quasi-static compression (as e.g. in Fig. 3) were used to correct the strain values measured by the mechanical testing machine. This is necessary because the precision to measure small strains is low. The actual strain rate in the quasi-static compression is approximately 5×10^{-5} s^{-1}. Uncertainties in the measurement and in the comparative analysis between the pristine and added sintered samples of the compression curves resides also in the following aspect: in the brittle fracturing-mode the defects induced by sample preparation (wire discharge cutting in this case) are important and can play the role of macroscopic flaws. Flaws in bending tests of dense (> 95 %) polycrystalline brittle engineering ceramics with additives less than 10-20 wt. %, as for our MgB_2 samples, are usually determined by the presence of large grains of the major phase [34]. The microstructure (at micron scale) of our samples is formed by MgB_2-colonies (i.e. sintered blocks of 40 - 120 μm [7]). Colonies contain a low amount of impurity phases and they are embedded into MgB_2 'dirty' regions with a high amount of secondary phases. Pristine or added samples are composites containing about 17 and 32 wt. % of impurity phases, respectively (Table 1). One observes that the difference is

roughly two-fold concerning the amount of secondary phases, but the compressive quasi-static parameters (E, σ_{max}, Table 1) are not much different. This result may indicate that indeed the MgB_2 sintered colonies are the key elements in flaws formation and fracturing behavior of the samples (see also *Section* 3.4). If this scenario is valid, a closer look on colonies is necessary. The carbon amount q substituting boron in the crystal structure of MgB_2 is higher in the added sample (Table 1). This is reflected (Table 1) by a smaller lattice parameter a (while c is almost constant) and a slightly higher residual strain of MgB_2. The signature of carbon substitution for boron is also revealed by a lower midpoint critical temperature, $T_{c,\ midpoint}$ for the added samples (Table 1). The $T_{c,\ midpoint}$ is estimated as the temperature at the half of the superconducting drop in the magnetization $m(T)$ curves (see Section 3.3). A higher Berkovich hardness was measured on the MgB_2 colonies for the added samples (Table 1). Yonezu and Chen [10] claim, based on indentation measurements, that the material stiffness in $MgB_{2-x}C_x$, yield stress, and fracture strength are degraded due to carbon additive, while the work hardening exponent is slightly higher. They concluded that the addition of C does not improve the mechanical properties of MgB_2. Apart from the carbon content, the relationship between the microstructure of the MgB_2 colony and mechanical properties has to be considered for pristine and added samples. In support of this idea, we note that the average crystallite size of MgB_2 in the two samples is slightly different (Table 1). But, again, this information should be carefully analyzed since Williamson-Hall procedure is not reliable for crystallite sizes above 100-150 nm.

Sintered samples show comparable values of Vickers hardness (Table 1). Fracture toughness, K_{IC}, (estimated based on Vickers indentation) is higher for the added samples. Microstructural details and C-substitution of MgB_2 contribute to this result. The presence of secondary phases as a result of SiC and Te addition can provide plasticity to the composite enhancing K_{IC} mainly through shortening of the cracks length by a deflection mechanism (*see Section 3.5*). This is apparently in contradiction with quasi-static compression test results: a lower plasticity was inferred for the added samples. The explanation for the encountered discrepancy resides in the scale and specific aspects of the measurement and in the composite nature of the samples. The composite nature and the scale of the material involved in the

indentation also explains the differences between Vickers or Berkovich hardness behavior: even when both measurements are performed on MgB_2, the colonies (and their surroundings) are different in the pristine and in the added samples. Situation is complex and further investigations are necessary. Some aspects are addressed in Section 3.5.

3.3 SHPB dynamic test on SPSed samples

This section is devoted to SHPB dynamic test results on MgB_2 SPSed samples, pristine and SiC-Te – added. The stress and strain histories (Fig. 4) of the MgB_2 specimens were calculated from the measured strain wave signals in the SHPB bars following refs. [35, 36].

The dynamic fracture stress at the 1st crack is of the order of 1200-1300 MPa (Fig. 4 a, b, Table 1). The strength and strain at the 1st crack, the strength and strain at the maximum stress are similar (Table 1) for pristine and added sample. It is well known that sample strain cannot be accurately measured in SHPB tests on hard ceramics given the deformation of the maraging steel bars and the short rising time in the initial stage of SHPB compression. We shall remind that a similar situation was encountered for the quasi-static case.

The compressive strength values of MgB_2 are lower than for other brittle and hard ceramics (Fig. 5). From the comparative analysis with experimental and simulated data for SiC-N [37], Al_2O_3 and AlN [38] one expects that compressive strength of MgB_2 is sensitive to stress rate above a typical critical (transitional) strain rate. According to [38] critical strain rate value is about 1000-1200 s^{-1} and it is common for many engineering brittle ceramics such as Al_2O_3 or SiC. Although our dynamic experiments were only performed for approximately one dynamic strain rate (~2500 s^{-1} and ~2800 s^{-1} for MgB_2-SPS and MgB_2+Te+SiC-SPS, respectively, Table 1), there is no reason to believe that MgB_2 is an exception to the rule. The dynamic strain rate $\dot{\varepsilon}_0$ was estimated as the average slope of the linear portion in the strain curve prior to the complete failure [35, 36, 39]. Values of $\dot{\varepsilon}_0$ position our SHPB dynamic test in the

defect-controlled region, based on classification: for quasi-static region $\dot{\varepsilon}_0$ < 250 s^{-1}, for defect controlled region 250 s^{-1}<$\dot{\varepsilon}_0$<25000 s^{-1}, and for kinetic region $\dot{\varepsilon}_0$>25000 s^{-1} [40].

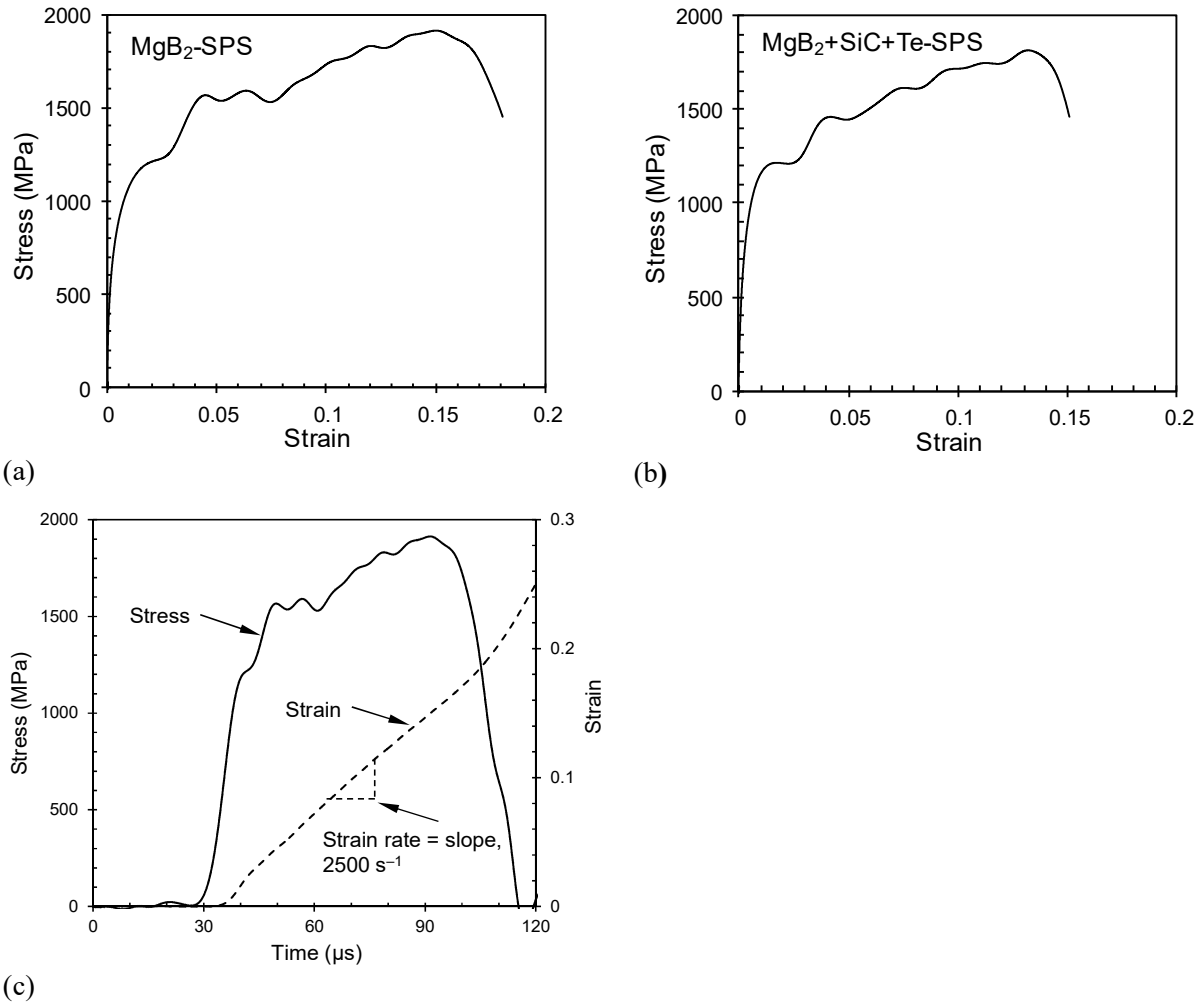

Fig. 4 Representative stress-strain curves in the SHPB measurement for SPSed samples: (a) pristine and (b) added; (c) stress and strain histories of sample MgB_2-SPS.

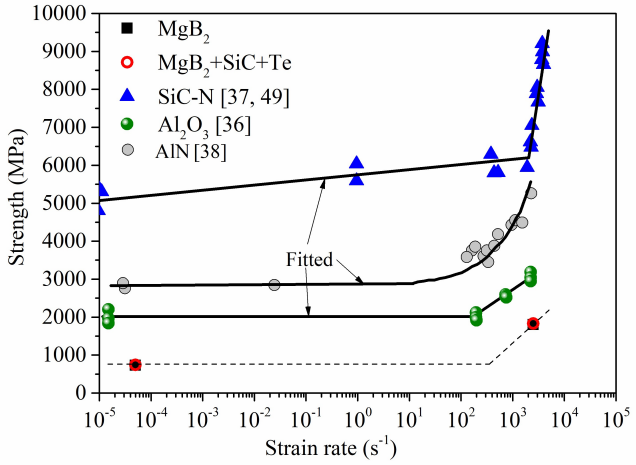

Fig. 5 Compressive strength against strain rate for MgB_2 and other engineering ceramics.

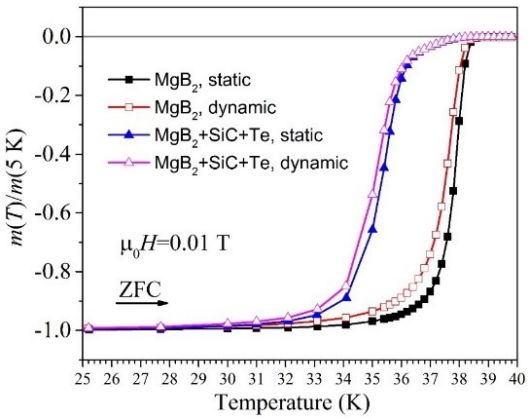

Fig. 6 Normalized $m(T)$ curves for SPSed samples before and after mechanical tests measured in zero-field-cooling conditions.

Regarding the defects possibly induced during SHPB, $m(T)$ curves (Fig. 6) measured on fragments after quasi-static compressive test and after SHPB show that the curves for the samples after SHPB are shifted to lower temperatures. The difference for each type of samples, pristine and added, in $T_{c,\ midpoint}$ (Table 1) is around 0.3 - 0.4 K. The decrease of $T_{c,\ midpoint}$ can be explained by introduction of defects in the dynamic experiments. In literature [41], the hard and brittle B_4C ceramic shows formation of amorphous regions under dynamic compressive loads. The idea that defects were induced in MgB_2 during SHPB needs further demonstrations and investigations. The problem resides in the fact that

magnetic measurements are performed on different samples that may show a certain degree of properties scattering.

3.4 Fragmentation aspects

Fragments of the samples after SHPB test were collected. They were approximated with a parallelepiped-like shape. Their size is smaller than for the fragments resulting after the compressive quasi-static test: in the quasi-static test there were fewer fragments and mostly of large size. We assume that this indicates on the loading rate effect on fragmentation for our dynamic conditions. This idea is also supported by arguments addressed in *Section 3.3*. The length (L) and width (W) of the fragments after SHPB test were measured (see *Section 2*), and their distribution is presented in Fig. 6. By fitting experimental data (Fig. 6) with (eq. 1) for MgB_2 we obtain the mean values $\mu_L = 47$ µm, $\mu_W = 47.4$ µm, while for MgB_2+SiC+Te the mean values are $\mu_L = 41.7$ µm and $\mu_W = 44.2$ µm. The arithmetic-mean-values of the measured W and L (Table 1) are 1.2-2 times larger than μ_L, and μ_W (Table 2). This can be considered acceptable since they show the same order or magnitude. Wang and Ramesh [37] discuss the problems in fragments size evaluation as being related to sampling technique which is associated with a size bias because the probability of the particle observance strongly depends on the size of the particle. According to Priest and Hudson [42], if the probability of observance of a bulk block is proportional to the size of the block, a negative exponential distribution changes into the shape of another distribution (lognormal). The dynamical fragmentation of the brittle materials follows a Poisson process, and in ref. [43, 44] was shown that fragments are generated with a negative exponential distribution. If so, one can apply directly the lognormal distribution (eq. 1) to fit experimental data.

The mean values of L, W, μ_L, and μ_W are comparable with the size of the MgB_2 colonies. This may suggest that colonies of MgB_2 are the key elements responding to dynamic stress load and contribute to formation of the axial fragmentation columns. This observation is complementary to the similar one for

the quasi-static compressive conditions from *Section 3.3*. Fractography details are presented in *Section 3.5* and they are supportive of such idea.

If we suppose that MgB_2 is a brittle ceramic-like material and fragmentation is accomplished based on a similar physical background and with similar statistical restrictions and approximations as for typical engineering ceramics [37], application of the fragmentation models to our data on MgB_2 should indicate on similar trends as for the engineering ceramics. Following this viewpoint, the width of the column formed as a result of axial cracks development within the wing crack array representation can be identified with the measured mean width (W *or* μ_w) of the observed fragments after SHPB. Fragmentation models considered for the fragment size calculation and analysis were Grady [45] (contributed also by Miller [46]), Glenn-Chudnovsky [47], and Drugan [48]. In the simulation of the fragment size we used $\dot{\varepsilon}_0$=2500 s^{-1}, i.e. a value close to our SHPB experimental conditions (Table 1), and $\dot{\varepsilon}_0$=10^5 s^{-1} that is the value usually considered in literature [48, 37]. We also included in our comparative analysis Al_2O_3 and SiC. Input parameters for Al_2O_3 and SiC are: σ_{max}=1 GPa, ρ=3900 Kg/m^3, υ=0.35, E=380 GPa, K_{Ic}=6 MPa·$m^{1/2}$, c=12.5·10^3 m/s [48], and σ_{max}=580 GPa, ρ=3200 Kg/m^3, υ=0.16, E=460 GPa, K_{Ic}=4.7 MPa·$m^{1/2}$, c=12·10^3 m/s [37], respectively.

The Grady model of dynamic fragmentation assumes that the local kinetic energy is balanced by the required energy for creating new surfaces [40]. Fragmentation to the columnar structure, that reflects the state developed after the macroscopic axial cracks are formed, depends on the strain rate and initial defects distribution. The fragment size (D_G) predicted by Grady model is:

$$D_G = \left(\frac{24 \cdot K_{IC}^2}{\rho^2 \cdot c^2 \cdot \dot{\varepsilon}_0^2}\right)^{\frac{1}{3}}, \text{[m]} \tag{3}$$

where: K_{Ic} is the material's plane strain fracture toughness (Pa·$m^{1/2}$), ρ is the mass density of the material (kg/m^3), c is the elastic wave speed (m/s, eq. 4), and $\dot{\varepsilon}_0$ is the strain rate (1/s). The elastic wave speed defined for one-dimensional plane strain deformations [46] is:

$$c = \sqrt{\frac{E}{\rho}}, \text{[m/s]} \tag{4}$$

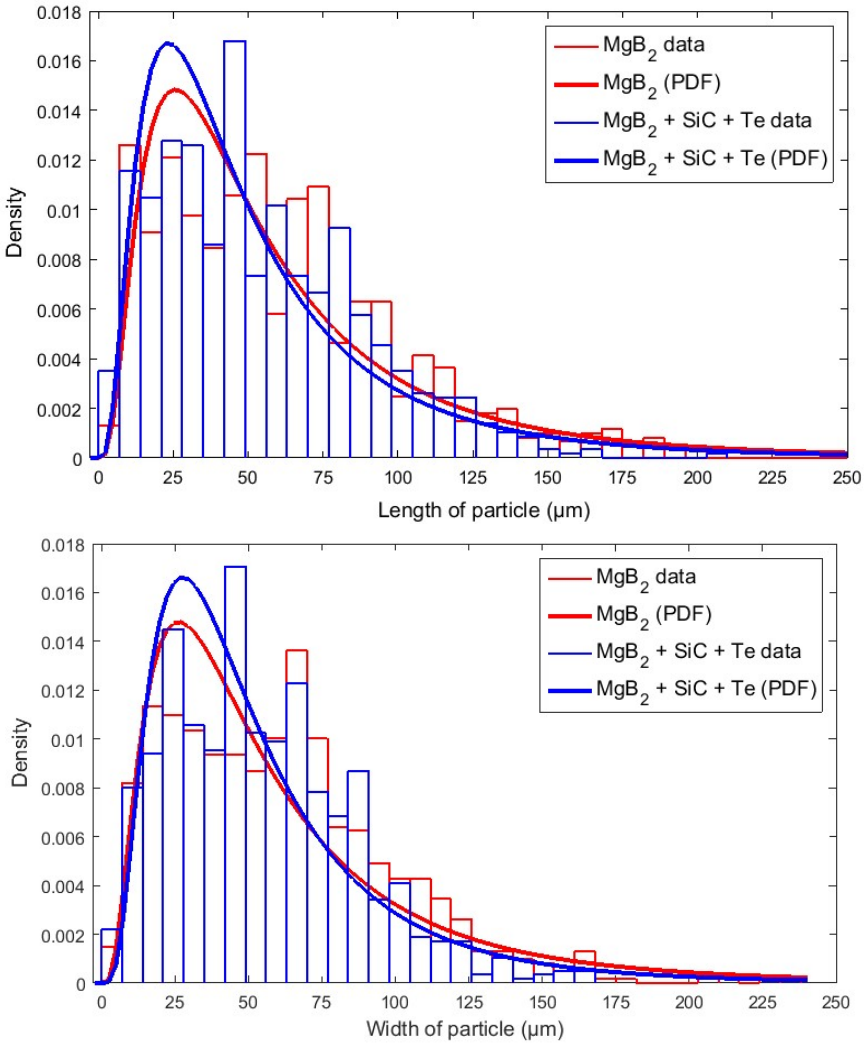

Fig. 6 Distribution of length (a) and width (b) of the fragments after SHPB test: experimental data and PDF curves obtained by fitting experimental data with (eq. 1).

The fragment size ($D_{G\text{-}C}$) according to Glenn and Chudnovsky [46, 47] is:

$$D_{G-C} = 4 \cdot \sqrt{\frac{\alpha}{3}} \cdot sinh\left(\frac{\theta}{3}\right), \text{[m]} \tag{5}$$

where

$$\theta = sinh^{-1}\left[\beta \cdot \left(\frac{3}{\alpha}\right)^{\frac{3}{2}}\right] \tag{6}$$

$$\alpha = \frac{3 \cdot \sigma_{max}^2}{\rho \cdot E \cdot \dot{\varepsilon}_0^{\,2}} \tag{7}$$

$$\beta = \frac{3}{2} \cdot \left(\frac{K_{Ic}}{\rho \cdot c \cdot \dot{\varepsilon}_0} \right)^2 \tag{8}$$

and σ_{max} is the strength value at which the loaded sample is fragmented. The G-C model considers the local kinetic energy and also the strain energy, hence, this approach leads to a different σ_{max} than in the Grady model.

Table 2 Fragmentation analysis of the samples after SHPB test: experimental and simulated data within different models. For a comparative analysis are presented also the data from literature for Al_2O_3 and SiC-N ceramics.

Sample		Fragment size [mm]					
	$\dot{\varepsilon}_0$ [1/s]	W / μ_w [mm]	D_G (Grady, eq. 3) [mm]	$D_{G\text{-}C}$ (Glenn-Chudnovsky, eq. 5) [mm]	D_D (Drugan) (eq. 9) [mm]	$D_{D\text{-quasi-static}}$ (Drugan quasi-static) (eq. 15) [mm]	$D_{G\text{-}C\text{-quasi-static}}$ (Glenn-Chudnovsky quasi-static) (eq. 16) [mm]
MgB_2	2500*	0.061/ 0.0474	5.422	0.0518	2.979	0.025	0.0519
	10^5	-	0.464	0.0518	0.255	0.051	0.0962
MgB_2+SiC +Te	2500*	0.055/ 0.0442	6.404	0.0962	1.743	0.051	0.0721
	10^5	-	0.548	0.0957	0.149	0.068	0.1396
Al_2O_3 [48]	2500*	-	3.875	0.0721	1.194	-	-
	10^5	-	0.331	0.0713	0.102	-	-
SiC-N [37]	2500*	-	3.86	0.1396	0.783	-	-
	10^5	-	0.33	0.1309	0.067	-	-

*with our parameters (see text)

Drugan [48] proposed the following expression for the fragment size:

$$D_D = a \cdot \tilde{\dot{\varepsilon}}_0^{\,-b}, \text{ [m]} \tag{9}$$

where a=2.1395, b=0.4264 for $\tilde{\dot{\varepsilon}}_0 \geq 0.9120$ (very high strain rates), and a=1.2999, b=0.66671 for $\tilde{\dot{\varepsilon}}_0 < 0.9120$ (our case).

$$\tilde{\varepsilon_0} = \frac{\dot{\varepsilon}_0 \cdot E \cdot \tau}{\sigma_{max}}, \text{ [m]} \tag{10}$$

Drugan model considers the cohesive zone model, i.e. fracture formation is a gradual phenomenon and consists in separation of the surfaces involved in the crack across an extended crack tip defined as the cohesive zone. Fracture is resisted by cohesive tractions. A critical time is necessary for the stress in the cohesive zone to attain the cohesive strength. Beyond this time, fragments stop expanding. Time dimension constant τ is given by:

$$\tau = \frac{\delta^* \cdot \hat{E}}{2 \cdot c \cdot \sigma_{max}}, \text{ [s]} \tag{11}$$

According to [48] δ^* value is derived by applying the J-integral to the cohesive zone model, for plane strain linear elastic fracture mechanics.

$$\delta^* = \frac{(1-\nu^2) \cdot K_{Ic}^2}{e \cdot E \cdot \sigma_{max}}, \text{ [m]} \tag{12}$$

where $\hat{E}$ [48] is the effective one-dimensional tensile modulus.

$$\hat{E} = \frac{E \cdot (1-\nu)}{(1+\nu) \cdot (1-2 \cdot \nu)}, \text{ [m]} \tag{13}$$

$$c = \sqrt{\frac{\bar{E}}{\rho}}, \text{ [m/s]} \tag{14}$$

In the quasi-static regime (Table 2), the Drugan and Glenn-Chudnovsky fragment sizes are not dependent on the strain rate:

$$D_{D-quasistatic} = \frac{e \cdot \delta^* \cdot \hat{E}}{\sigma_{max}}, \text{ [m]} \tag{15}$$

$$D_{(G-C-\ quasistatic} = \frac{4 \cdot \beta}{\alpha}, \text{ [m]} \tag{16}$$

(α and β are defined in eq. 7, 8).

Another quasi-static model assumes that the minimum fragment size can be approximated with (eq. 17)

$$D_{quast} = 0.02 \cdot e = 0.054, \text{ [mm]} \quad (17)$$

where $e=2.718$ is the Euler's number [48].

From Table 2, one observes that calculated values of D for Glenn-Chudnovsky model under dynamic load conditions approach the experimental mean values. Drugan model apparently works well for $\dot{\varepsilon}_0=10^5\,s^{-1}$, but provides values quite far from the experimental ones for $\dot{\varepsilon}_0=2500\,s^{-1}$. The cohesive zone model considered in the Drugan approximation predicts the behavior of the uncracked structures, including those with blunt notches. Results may suggest that initial cracks or defects (e.g. inclusions) acting as favorable sites (stress concentrators) for the wing cracks formation are important and can provide the argument for a better approximation with G-C model of the experimental data in a polycrystalline ceramic, and in a MgB_2 composite material for our particular case. Microstructural details may influence fragmentation processes, but this should be placed in the context of the scale. Although in the next *Section 3.4* we shall observe some intergranular fracturing, size of the resulting fragments is much higher than the grain size (≤1 μm, Fig. 7 and see also Table 1 for crystallite size of MgB_2). Our observations are in good agreement with those for SiC [37] and it can be appreciated that the fragmentation steps under dynamic compressive load are similar for both materials: (i) micro crack development (nucleated cracks grow/propagate and their coalescence); (ii) macro crack coalescence and axial splitting; (iii) the collapse of the material in the split process; (iv) disintegration into final fragments. Inertial effects influence the crack growth bringing material to its strength level in step (i), provides the axial columnar structure defined by longitudinal cracks in step (ii) and material breakage in step (iii) with further fragmentation in step (iv) due to local kinetic and strain energy.

3.5 Fractography analysis of the samples after quasi-static and SHPB tests

As already mentioned in Section 3.3, our MgB_2 SPSed samples are composites containing secondary phases such as MgO, MgB_4, higher Mg-borides and/or boroxides [7]. In the added samples are also present the phases Mg_2Si and MgTe [21]. Secondary phases are located (Fig. 7 f, p) at the grain boundaries or at the triple points. They are of small size, often in the nano range (10-150 nm). Microstructure shows the presence of relatively clean well sintered MgB_2 blocks (colonies) embedded into a 'dirty' matrix of MgB_2 with many impurities [7]. We also remind that in the added sample MgB_2+SiC+Te-SPS, a higher amount of C substitutes for B in the crystal lattice of MgB_2 (Table 1). Structural and microstructural encountered differences can contribute to mechanical behavior of the pristine and added samples and the evidence of these differences are revealed by fractography observations.

The fragments' surface after quasi-static compressive test on sintered samples has a higher roughness for the added sample (Fig. 7 m) than for pristine sample (Fig. 7 c). This observation points on a higher ductility of the added sample than of the pristine one. The result is in good agreement with a higher quasi-static fracture toughness, K_{Ic} for the added sample (Table 1). Although less obvious, surface analysis of the fragments after dynamic test apparently shows a similar tendency (compare Fig. 7 d, e with Fig. 7 n, o). The reason for a higher plasticity in the doped sample is related to fracturing mechanisms. In Fig. 7 a, b for pristine sample, the width of the crack is small, its edges are rather flat and wavy, while for added sample the crack width is large and the crack is composed of more and shorter straight segments (Fig. 8 b) that provides a stronger fractal appearance. Therefore, deflection of the crack can be observed for both samples, but it is stronger in the added sample. Often the angles between the straight segments composing the fractal-like crack are of 60 or 120°. Taking into account that the crystal structure of MgB_2 is hexagonal, it is inferred that in the added sample there is a stronger contribution of the intergranular fracture mechanism. This mechanism produces a 'pull out' of the MgB_2 grains and this can be observed for both investigated samples and mechanical quasi-static and dynamic tests (Fig. 7 b, e,

k, o). We speculate that the presence of a higher amount of secondary phases from the added sample promotes and explains higher plasticity of this sample under quasi-static and dynamic loads. Nevertheless, as addressed in Section 3.2, contribution of carbon should be also considered especially for the added sample for which addition of SiC is a source of carbon: carbon can influence the grain boundaries and also the MgB_2 grains through the chemical substitution of B. Carbon at grain boundaries may provide additional plasticity through the intergranular mechanism, but residual strain (that is higher for C-doped MgB_2, Table 1) may increase hardness of the grains as in our case (see Berkovich hardness, Table 1). The increased hardness of the MgB_2 grains will be reflected on the brittle transgranular fracturing of MgB_2.

Presented observations indicate that the ratio between intergranular and transgranular (intragranular) fracture is different and it is in the direction of a stronger intergranular fracturing for the added sample. The evidence that transgranular fracturing is active in our samples and it is the main mechanism, especially for the MgB_2 blocks (colonies), is given by flat and smooth surfaces of fracture that can be visualized in Fig. 8a. Assumption from Sections 3.3 and 3.5 that MgB_2 blocks may play a key role in fragmentation (fragment size) in the compressive fracturing processes is supported. Fig. 8a also shows that transgranular fracturing of the MgB_2 blocks is contributed by the closed sintering pores.

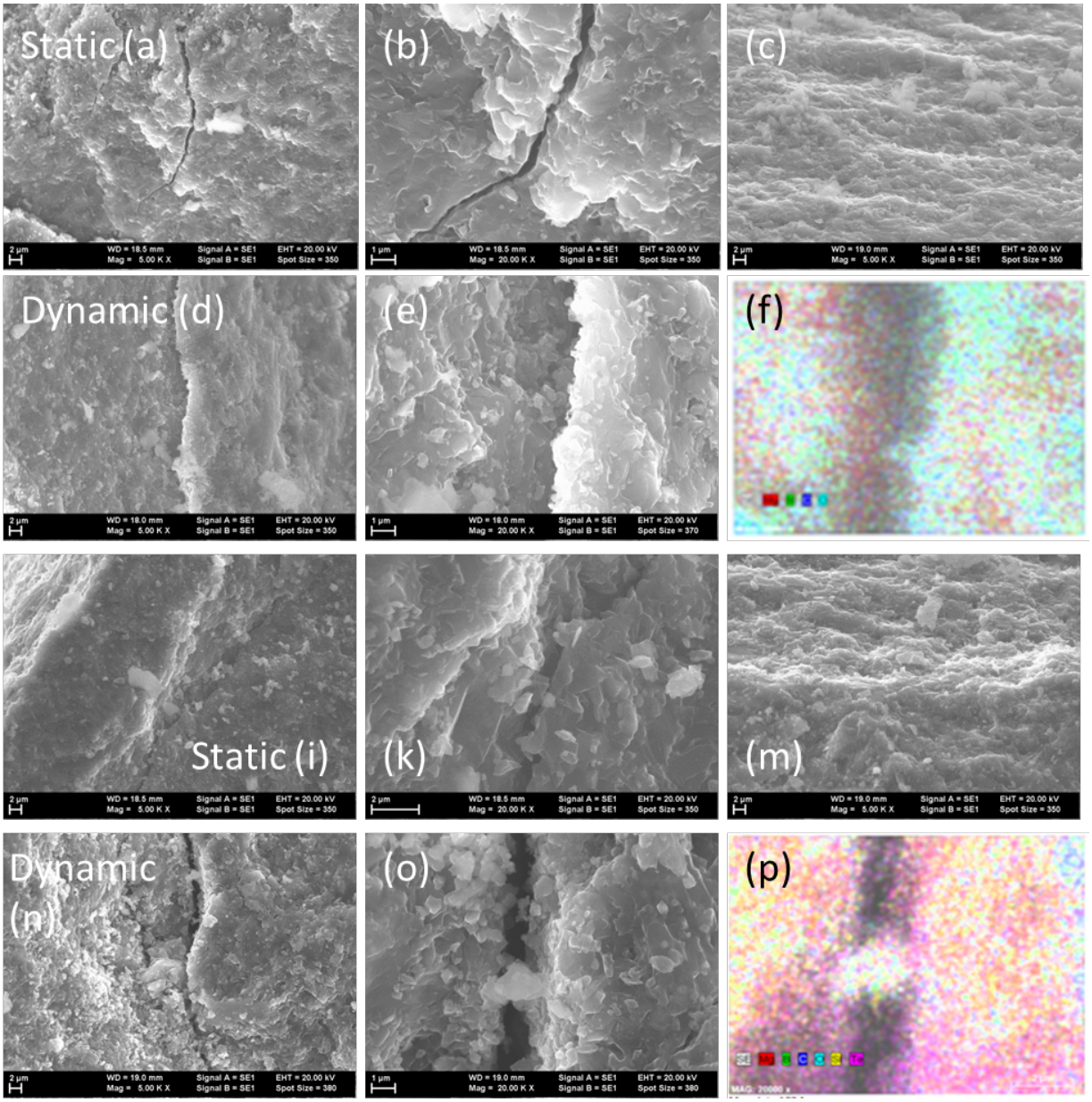

Fig. 7 SEM images: (a)-(f) and (i)-(p) are for pristine and added SPSed samples, respectively, after quasi-static ((a)-(c), (i)-(m)) and dynamic ((d)-(f), ((n)-(p)) compressive tests. In (f) and (p) are red-blue-green images of overlapped EDS elemental maps for detected elements.

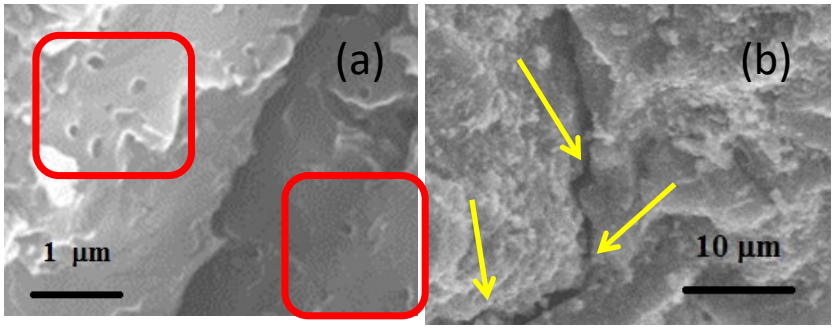

Fig. 8 SEM images taken on: (a) pristine SPSed sample after quasi-static compressive test showing intragranular fracture (see rectangles) of large MgB_2 sintered blocks containing closed pores and on (b) added SPSed sample after SHPB test. With arrows are indicated fractal-type crack-deflection.

4. Conclusion

Compresive mechanical properties of pristine and (SiC+Te)-added MgB_2 powders, green and SPSed compacts were investigated. The amount of the additive (SiC+Te) was optimum for maximization of the functional parameters (J_c and H_{irr}) of high density (> 95%) bulk MgB_2 processed by spark plasma sintering [21]. Some differences between samples were revealed and discussed. Additives provide plasticity to the system although some mechanical and fragment size parameters almost does not change (tan δ, σ, Vickers hardness, W, L, μ_W, μ_L). We observed for the bulk SPSed samples that the ratio of intergranular to transgranular fracturing ratio changes, the first one being stronger in the added sample. Thus, the quasi-static K_{IC} is higher for the added sample. However, sintered samples are brittle and show roughly similar fragmentation behavior as other brittle engineering ceramics. In this process, the composite nature of our samples should be considered with a special attention on MgB_2 blocks (colonies) that provide the major contribution to fracturing. This idea needs further confirmation. The Glenn-Chudnovsky model of fracturing under dynamic load generates the closest values of fragment size to our experimental data.

Acknowledgements

Authors acknowledge MEI-UEFISCDI, Romania, projects POC 37_697, No. 28/ 01.09.2016 REBMAT, and COFUND-M-ERA.NET II-BIOMB, No. 74 / 14.06.2017.

References

[1] N. Nagamatsu, N. Nakagawa, T. Muranaka, Y. Zenitani, J. Akimitsu, Superconductivity at 39 K in magnesium diboride, Nature 410 (2001) 63.

[2] D. Batalu, A. M. Stanciuc, L. Moldovan, G. Aldica, P. Badica, Evaluation of pristine and Eu_2O_3-added MgB_2 ceramics for medical applications: hardness, corrosion resistance, cytotoxicity and antibacterial activity, Mat. Sci. Engineering. C 42 (2014) 350.

[3] T. A. Prikhna, W. Gawalek, A. B. Surzhenko, V. E. Moshchil, N. V. Sergienko, Ya. M. Savchuk, V. S. Melnikov, P. A. Nagorny, T. Habisreuther, S. N. Dub, M. Wendt, D. Litzkendorf, J. Dellith, Ch. Schmidt, G. Krabbes, A. V. Vlasenko, High-pressure synthesis of MgB_2 with and without tantalum additions, Physica C 372-376 (2002) 1543.

[4] O. Gorur, M. Nursoy, C. Terzioglu, A. Varilci, I. Belenli, Influence of annealing temperature on the microstructure and mechanical properties of MgB_2, Journal of Physics: Conference Series 153 (2009) 012012.

[5] S. Safran, A. Kılıc¸ E. Asikuzun, E. Kılıcarslan, O. Ozturk, A. Gencer, Influence of different boron precursors on superconducting and mechanical properties of MgB_2, J. Mater. Sci.: Mater. Electron. 25 (2014) 2737.

[6] O. Ozturk, E. Asikuzun, S. Kaya, Significant change in micro mechanical, structural and electrical properties of MgB_2 superconducting ceramics depending on argon ambient pressure and annealing duration, J. Mater. Sci.: Mater. Electron. 26 (2015) 3840.

[7] G. Aldica, D. Batalu, S. Popa, I. Ivan, P. Nita, Y. Sakka, O. Vasylkiv, L. Miu, I. Pasuk, P. Badica, Spark plasma sintering of MgB_2 in the two-temperature route, Physica C 477 (2012) 43.

[8] C. E. J. Dancer, D. Prabhakaran, M. Basoglu, E. Yanmaz, H. Yan, M. Reece, R. I. Todd, C. R. M. Grovenor, Fabrication and properties of dense ex situ magnesium diboride bulk material synthesized using spark plasma sintering, Supercond. Sci. Technol. 22 (2009) 095003.

[9] N. Guclu, Micro-indentation study of Mg-addition MgB_2 superconducting wires, Journal of Alloys and Compounds 509 (5) (2011) 1691.

[10] A. Yonezu, Xi Chen, Evaluation of critical strain for crack nucleation of magnesium di-boride superconductor using indentation method, Materials Chemistry and Physics 125 (3) (2011) 528.

[11] M. Egilmez, L. Ozyuzer, M. Tanoglu, S. Okur, O. Kamer, Y. Oner, Electrical and mechanical properties of superconducting MgB_2/Mg metal matrix composites, Supercond. Sci. Technol. 19 (2006) 359.

[12] G. Giunchi, T. Cavallin, P. Bassani, S. Guicciardi, The mechanical properties of the MgB_2 bulk materials obtained by reactive liquid Mg infiltration, AIP Conference Proceedings 986 (2008) 396.

[13] A. Murakami, H. Teshima, T. Naito, H. Fujishiro, T. Kudo, Mechanical properties of MgB_2 bulks, Physics Procedia 58 (2014) 98.

[14] M. Muralidhar, K. Inoue, M. R. Koblischka, A. Murakami, M. Murakami, Effects of Silver Addition on Critical Current Densities and Mechanical Properties in Bulk MgB_2, Advanced Engineering Materials 17 (6) (2015) 831.

[15] A. K. M. A. Islam, F. N. Islam, Ab initio investigation of elastic constants of superconducting MgB_2, Physica C 363 (3) (2001) 189.

[16] V. Milman, M. C. Warren, Elastic properties of TiB_2 and MgB_2, J. Phys.: Condens. Matter. 13 (24) (2001) 5585.

[17] P. Ravindran, P. Vajeeston, R. Vidya, A. Kjekshus, H. Fjellvåg, Detailed electronic structure studies on superconducting MgB_2 and related compounds, Phys. Rev. B 64 (2001) 224509.

[18] V. F. Nesterenko, Y. Gu, Elastic Properties of Hot Isostatically Pressed Magnesium Diboride, Applied Physics Letters 82 (23) (2003) 4104.

[19] T. Ichitsubo, H. Ogi, S. Nishimura, T. Seto, M. Hirao, H. Inui, Elastic stiffness and ultrasonic attenuation of superconductor MgB2 at low temperatures, Phys. Rev. B 66 (2002) 052514.

[20] U. Harms, A. Serquis, R. B. Schwarz, V. F. Nesterenko, Low Temperature Elastic Constants of Polycrystalline MgB_2, J. Supercond. Nov. Mag. 16 (2003) 941.

[21] G. Aldica, S. Popa, M. Enculescu, P. Badica, Te and SiC co-doped MgB_2 obtained by an ex situ spark plasma sintering technique, Scripta Materialia 68 (2013) 428.

[22] S. X. Dou, S. Soltanian, J. Horvat, X. L. Wang, S. H. Zhou, M. Ionescu, H. K. Liu, Enhancement of the critical current density and flux pinning of MgB_2 superconductor by nanoparticle SiC doping, Appl. Phys. Lett. 81 (2002) 3419.

[23] G. Aldica, S. Popa, M. Enculescu, P. Badica, Enhancement of critical current density and irreversibility field by Te or TeO_2 addition to MgB_2 bulk processed by spark plasma sintering, Scripta Materialia 66 (2012) 570.

[24] V. Sandu, G. Aldica, S. Popa, M. Enculescu, P Badica, Tellurium addition as a solution to improve compactness of ex-situ processed MgB_2-SiC superconducting tapes, Supercond. Sci. Technol. 29 (2016) 065012.

[25] G. W. Marks, L. A. Monson, Effect of Certain Group IV Oxides on Dielectric Constant and Dissipation Factor of Barium Titanate, Ind. Eng. Chem. 47 (1955) 1611.

[26] L. Lutterotti, Total pattern fitting for the combined size–strain–stress–texture determination in thin film diffraction, Nuclear Instruments and Methods in Physics Research Section B 268 (2010) 334-340.

[27] G. K. Williamson, W. H. Hall, X-ray line broadening from filed aluminium and wolfram, Acta Metallurgica 1 (1953) 22-31.

[28] L. S. Walker, V. R. Marotto, M. A. Rafiee, N. Koratkar, E. Corral, Toughening in graphene ceramic composites, ACS Nano 5 (2011) 3182.

[29] A. K. Suri, C. Subramanian, J. K. Sonber, T. S. R. Ch. Murthy, Synthesis and consolidation of boron carbide: a review, International Materials Reviews 55 (2010) 4.

[30] S. H. Risbud, J. R. Groza, M. J. Kim, Clean grain boundaries in aluminum nitride ceramics densified without additives by a plasma-activated sintering process, Philosophical Magazine B-Physics of Condensed Matter, Statistical Mechanics, Electronic, Optical and Magnetic Properties 69 (1994) 525.

[31] H. Zhao, G. Gary, On the use of SHPB techniques to determine the dynamic behavior of materials in the range of small strains, International Journal of Solids and Structures, 33 (1996) 3363-3375.

[32] G. Aldica, S. Popa, M. Enculescu, D. Batalu, L. Miu, M. Ferbinteanu, P. Badica, Addition of Ho_2O_3 of different types to MgB_2 in the ex-situ Spark Plasma Sintering: Simultaneous control of the critical current density at low and high magnetic fields, Materials Chemistry and Physics 146 (2014) 313.

[33] J. D. DeFouw, D. C. Dunand, Superplastic compressive flow in MgB2, Acta Materialia 57 (2009) 4745.

[34] O. Vasylkiv, D. Demirskyi, P. Badica, T. Nishimura, A.I.Y. Tok, Y. Sakka, H. Borodianska, Room and high temperature flexural failure of spark plasma sintered boron carbide, Ceramics International 42 (2016) 7001.

[35] Z. Wang, P. Li, Characterisation of dynamic behaviour of alumina ceramics: evaluation of stress uniformity, AIP Advances 5 (10) (2015) 107224.

[36] Z. Wang, P. Li, Dynamic failure and fracture mechanism in alumina ceramics: Experimental observations and finite element modelling, Ceramics International 41 (2015) 12763.

[37] H. Wang, K. T. Ramesh, Dynamic strength and fragmentation of hot-pressed silicon carbide under uniaxial compression, Acta Materialia 52 (2) (2004) 355.

[38] G. Ravichandran, G. Subhash, A micromechanical model for high strain rate behavior of ceramics, International Journal of Solids and Structures 32 (17–18) (1995) 2627.

[39] P. Li, Z. Wang, Experimental Characterization and Modified Constitutive Modeling of the Strain Rate Dependent Compressive Behavior of Adhesives, Macromol. Mater. Eng. 301 (5) (2016) 577−585.

[40] F. Zhou, J.-F. Molinari, K. T. Ramesh, A cohesive model based fragmentation analysis: effects of strain rate and initial defects distribution, International Journal of Solids and Structures 42 (2005) 5181.

[41] M. Chen, J. W. McCauley, K. J. Hemker, Shock-induced localized amorphization in boron carbide, Science 299 (2003) 1563.

[42] S. D. Priest, J. A. Hudson, Estimation of discontinuity spacing and trace length using scanline surveys, Int. J. Rock Mech. Min. Sci. Geomech. Abstr. 18 (3) (1981) 183.

[43] D. E. Grady, M. E. Kipp, Geometric statistics and dynamic fragmentation, J. Appl. Phys. 58 (1985) 1210.

[44] D. E. Grady, Particle size statistics in dynamic fragmentation, J. Appl. Phys. 68 (1990) 6099.

[45] D. E. Grady, Local inertial effects in dynamic fragmentation, J. Appl. Phys. 53 (1982) 322.

[46] O. Miller, L. B. Freund, A. Needleman, Modeling and Simulation of Dynamic Fragmentation in Brittle Materials, Int. J. Fracture 96 (2) (1999) 101.

[47] L. A. Glenn, A. Chudnovsky, Strain-energy effects on dynamic fragmentation, J. Appl. Phys. 59 (1986) 1379.

[48] W. J. Drugan, Dynamic fragmentation of brittle materials: analytical mechanics-based models, J. Mech. Phys. Solids 49 (6) (2001) 1181.

[49] J. Lankford, High strain rate compression and plastic flow of ceramics, J. Mater. Sci. Lett. 15 (1996) 745.